

UC Santa Barbara

UC Santa Barbara Previously Published Works

Title

Direct Pyrolysis of a Manganese-Triazolate Metal–Organic Framework into Air-Stable Manganese Nitride Nanoparticles

Permalink

<https://escholarship.org/uc/item/6rv9d2bt>

Journal

Advanced Science, 8(4)

ISSN

2198-3844

Authors

Hu, Yating
Li, Changjian
Xi, Shibo
et al.

Publication Date

2021-02-01

DOI

10.1002/advs.202003212

Peer reviewed

Direct Pyrolysis of a Manganese-Triazolate Metal–Organic Framework into Air-Stable Manganese Nitride Nanoparticles

Yating Hu, Changjian Li, Shibo Xi, Zeyu Deng, Ximeng Liu, Anthony K. Cheetham,* and John Wang*

Although metal–organic frameworks (MOFs) are being widely used to derive functional nanomaterials through pyrolysis, the actual mechanisms involved remain unclear. In the limited studies to date, elemental metallic species are found to be the initial products, which limits the variety of MOF-derived nanomaterials. Here, the pyrolysis of a manganese triazolate MOF is examined carefully in terms of phase transformation, reaction pathways, and morphology evolution in different conditions. Surprisingly, the formation of metal is not detected when manganese triazolate is pyrolyzed in an oxygen-free environment. Instead, a direct transformation into nanoparticles of manganese nitride, Mn_2N_x embedded in N-doped graphitic carbon took place. The electrically conductive Mn_2N_x nanoparticles show much better air stability than bulk samples and exhibit promising electrocatalytic performance for the oxygen reduction reaction. The findings on pyrolysis mechanisms expand the potential of MOF as a precursor to derive more functional nanomaterials.

applications in energy storage or electrocatalysis.^[1] During a typical MOF pyrolysis process, metallic nanoparticles, or even nanoclusters containing just a few atoms, are initially formed as the organic linkers are lost.^[2] For metals with a reduction potential of less than -0.27 V, metal oxide nanoparticles may become the final product, when the MOF linker contains oxygen.^[3] Alternatively, metal carbide nanoparticles can be formed when the MOF-derived metallic species react with the carbon that forms from the organic linkers (e.g., at a temperature of higher than 1600 °C, MOF-derived Co metal nanoparticles react with carbon to form Co_3C).^[4] When the metallic species are removed without undergoing further reaction, porous carbons can be left behind.^[5] These MOF-derived carbonaceous or metal-based nanomaterials show

Metal–organic frameworks (MOFs) formed by linking inorganic and organic building units have emerged as versatile precursors for obtaining carbonaceous or metal-based nanomaterials for

great potential in energy-related fields due to the high electrical conductivity provided by the carbon combined with the uniformly distributed active sites.^[6] In some cases, the uniform pores arising from the MOF precursor are used as a constraint, preventing agglomeration and coalescence of the in situ generated nanocrystals.^[7] Although various metals/metal oxides and porous carbons can be derived from MOFs through pyrolysis and further treatment,^[2c,8] the mechanisms involved in MOF pyrolysis remain unclear in many respects. Furthermore, to the best of our knowledge, there is no report of a one-step reaction that transforms the MOF into a transition metal compound while making simultaneous use of both the metal ion and the organic linker in the MOF.


Transition metal nitrides (TMNs) exhibit higher electrical conductivities than the corresponding oxides and higher stabilities than the carbides during electrocatalytic reactions, such as in oxygen reduction reactions (ORR).^[9] Upon forming nitride, the transition metal's filled state of d-band is narrowed and unfilled state broadened. As a result, the surface of TMN is more catalytically active than its parent metal or corresponding transition metal oxides, even more active than the benchmarking Pt group metals for reactions that involve the donation of bonding electrons.^[10] Generally, an effective electrocatalyst requires a high surface area and reasonable electrical conductivity. Reducing the particle size of a material to the nanoscale (i.e., smaller than 50 nm) is an effective way to increase the surface area, thereby increasing the number of accessible catalytic sites.^[11] Recently,

Dr. Y. Hu, Dr. C. Li, Dr. Z. Deng, X. Liu, Prof. A. K. Cheetham, Prof. J. Wang
Department of Materials Science and Engineering
National University of Singapore
9 Engineering Drive 1, Singapore 117574, Singapore
E-mail: akc30@cam.ac.uk; msewangi@nus.edu.sg

Dr. Y. Hu
Function Hub
Hong Kong University of Science and Technology (Guangzhou)
S&T Building, Nansha IT Park, Guangzhou 511458, China

Dr. S. Xi
Institute of Chemical and Engineering Sciences
Agency for Science, Technology and Research (A*STAR)
1 Pesek Road, Jurong Island, Singapore 627833, Singapore

Prof. A. K. Cheetham
Materials Research Laboratory
University of California
Santa Barbara, CA 93106, USA

 The ORCID identification number(s) for the author(s) of this article can be found under <https://doi.org/10.1002/advs.202003212>

© 2021 The Authors. *Advanced Science* published by Wiley-VCH GmbH. This is an open access article under the terms of the Creative Commons Attribution License, which permits use, distribution and reproduction in any medium, provided the original work is properly cited.

DOI: 10.1002/advs.202003212

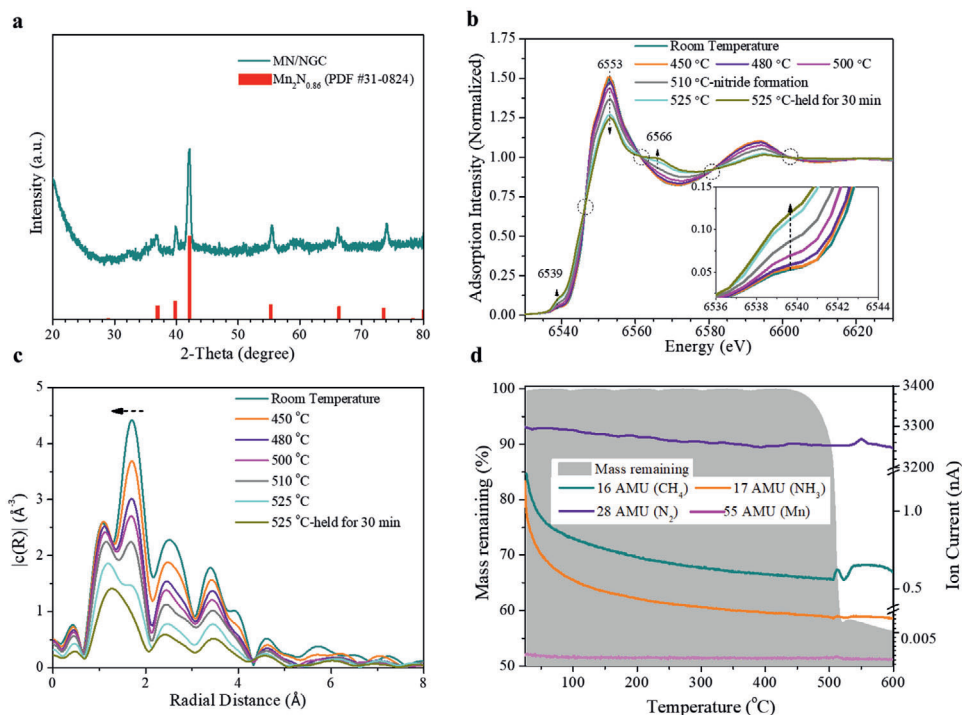


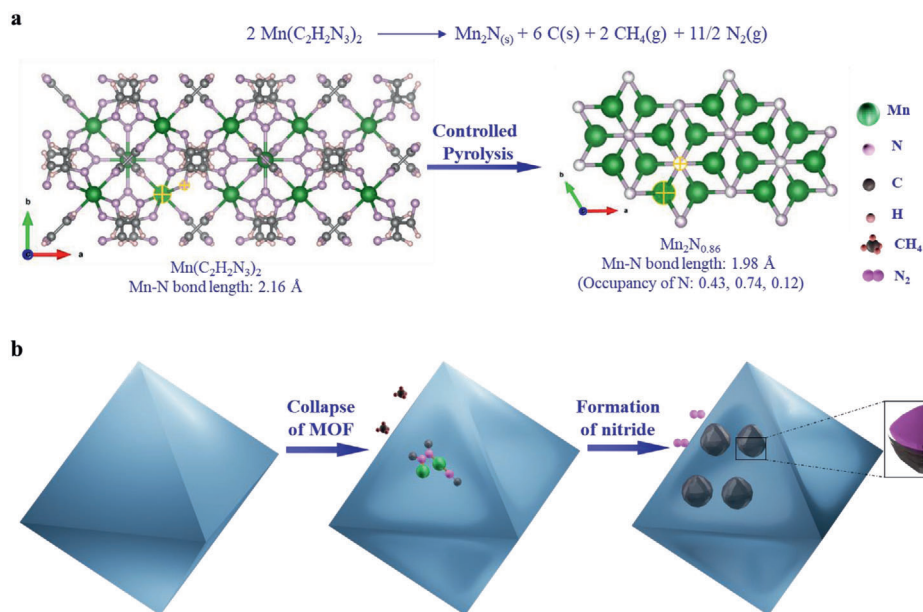
Figure 1. The phase transformation during the pyrolysis of manganese triazolate in pure N_2 . a) XRD of the as-obtained pyrolysis product MN/NGC. b) In situ Mn K-edge X-ray absorption near-edge structure (XANES) spectra and c) Fourier transform of the extended X-ray absorption fine structure (EXAFS) spectra during the pyrolysis of manganese triazolate's into manganese nitride (heating up at 5 °C min^{-1} ramp in N_2 from room temperature, then held for 30 min at 525 °C). d) Thermogravimetric analysis-mass spectrometry (TG-MS) results during the pyrolysis of manganese triazolate in N_2 , ramping at 5 °C min^{-1} .

sub-micrometer-scale transition metal nitrides have been synthesized by nitridation of oxides in ammonia, or using the $-NH_2$ or $-NH_4$ containing precursors such as urea.^[11] In this way, Co nitrides with various morphologies^[6,12] as well as NiN_3 ,^[13] TiN ,^[14] and VN ^[15] have been synthesized. However, the reported ones are either relatively large in size (sub-micrometer scale rather than nano) or lack in uniformity of size and morphology. The synthetic methods are mainly limited to the utilization of ammonia, which poses safety and environmental issues. In addition, nanoscale TMNs with higher specific surface area are difficult to obtain and stabilize as they are easily oxidized, either during their synthesis or storage.^[16] Review articles have pointed out that a better preparation method for nanoscale TMNs, especially those to be used in electrocatalysis, is urgently needed.^[15,11]

Herein, we studied the pyrolysis of a manganese 1,2,3-triazolate MOF $Mn(C_2N_3H_2)_2$,^[17] under several different conditions. Interestingly, one of them leads to the formation of air-stable manganese nitride nanoparticles, $\approx 30\text{ nm}$ in diameter, enclosed in graphitic carbon layers. The reaction mechanism has been studied by probing the phase transitions, morphology evolution, and chemical reactions involved during the pyrolysis. The manganese nitride nanoparticles show superior stability in air compared to bulk samples, mainly due to the existence of the graphitic carbon layers in which the nitride nanoparticles are enclosed and the appropriate size match between the two. The high electrical conductivity and stability of the nitride nanocrystals uniformly distributed on a carbon monolith results

in better ORR electrocatalytic activity than that of manganese oxide nanomaterials.

The pyrolysis of a MOF is the thermal decomposition process involving bond breaking and transformation of the organic linker into smaller organic molecules and carbon.^[2c] The atmosphere used during pyrolysis plays an important role in the process, as do the heating ramp rate, holding temperature, and duration. When a manganese MOF with an oxygen-containing organic linker is pyrolyzed, a manganese oxide is usually the final product due to Mn's high affinity toward oxygen.^[8c,18] For this reason, the oxygen-free/nitrogen-containing manganese triazolate (MOF MET-2) was chosen as the precursor to obtain manganese nitride.^[17] To understand the mechanism of MOF pyrolysis, various in situ and ex situ characterization tools were employed. First, thermogravimetric analysis (TGA) of the manganese triazolate in flowing N_2 gas (Figure S1a, Supporting Information) shows a mass loss at around 500 °C when the ramp rate is 5 °C min^{-1} or higher. At higher ramp rate (e.g., 10 or 30 °C min^{-1} compared to 5 °C min^{-1}), the mass loss is significantly increased. The remaining mass is less than the content of manganese in MOF, indicating a likely formation of organometallic compound. The pyrolysis/annealing of the manganese triazolate was therefore carried out in flowing N_2 using a tube furnace (ramp from room temperature in 5 °C min^{-1} and then hold at various temperatures from 500 to 700 °C). Powder X-ray diffraction (XRD) analysis in Figure 1a revealed that crystalline Mn_2N_x ($x = 0.86$) is formed from



Scheme 1. Reaction pathway and morphology change from manganese triazolate to manganese nitride nanoparticles. a) Proposed overall reaction and the crystal structures of $\text{Mn}(\text{C}_2\text{H}_2\text{N}_3)_2$ (0.5 unit cell) and $\text{Mn}_2\text{N}_{0.86}$. b) Illustration of the morphology evolution during the pyrolysis.

the pyrolysis/annealing at 525 °C for 4 h, in highly purified N_2 atmosphere. Sample obtained from pyrolysis/annealing at 525 °C for 4 h is coded as MN/NGC (MN stands for manganese nitrides and NGC stands for N-doped graphitic carbon, which will be further discussed). Through examining the pyrolyzed products obtained from various heat treatments conducted in the tube furnace, it is found that the manganese triazolate is highly sensitive to air at higher temperatures (>400 °C). Pure Mn_2N_x can only be formed when an oxygen trap is attached to the N_2 gas hose; this reduces the oxygen content to less than 50 ppb, compared to up to 2 ppm in the gas taken directly from the commercial N_2 cylinder. A mixture of MnO and Mn_2N_x or highly crystalline MnO is obtained when the oxygen trap is removed or when the pyrolysis is done in air, respectively (Figure S2, Supporting Information).

In situ Mn K-edge X-ray absorption fine structure (XAFS, including both XANES and EXAFS) spectra were measured during the pyrolysis of manganese triazolate in highly purified N_2 gas to shed further light on the reaction mechanism. Data were collected while the manganese triazolate was heated from room temperature with a ramp rate of 5 °C min^{-1} under highly purified N_2 gas flowing at 100 mL min^{-1} . The XANES data collected at 200, 300, and 400 °C show no change (Figure S3, Supporting Information) because the manganese triazolate is thermally stable up to 400 °C (Figure S4, Supporting Information).^[17] Furthermore, the XANES profiles at 450 and 480 °C show negligible differences from the one at room temperature (Figure 1b). Starting from 510 °C, however, the intensity of the peak at 6539 eV increases significantly. This pre-edge peak, which is about 10 eV below the main peak, corresponds to an electronic excitation from 1s to 3d for first-row transition metals.^[19] The peak becomes more intense when the coordination environment of the metal atom is distorted from a centrosymmetric to a non-centrosymmetric one.^[20] None of the manganese oxides show a

peak at this energy.^[21] In this case, the pre-edge peak at 6539 eV is associated with the formation of manganese nitride Mn_2N_x ^[19] because the symmetry at the Mn site is non-centrosymmetric due to the presence of adjacent nitrogen vacancies (**Scheme 1a**). The relative intensity of the pre-edge peak compared with the main adsorption peak at 6553 eV increases when temperature is raised above 500 °C, as the manganese environment gradually changes from the centrosymmetric coordination in manganese triazolate^[17] to the non-centrosymmetric environment in Mn_2N_x . The clear-cut intersection points of the curves (isosbestic points) are evidences of the transformation between two phases (manganese triazolate to $\text{Mn}_2\text{N}_{0.86}$), taking place during the heat treatment. The overall peak profile, especially the post-edge peak at 6566 eV which becomes obvious at 525 °C, matches the reported peaks for manganese in manganese nitrides.^[22] The peak at 6553 eV that remained throughout the pyrolysis, and the absence of a peak at 6580 eV, exclude the formation of various manganese oxides^[23] and metallic manganese.^[22] To underline this point, the in situ XANES results, especially the isosbestic points, confirm that when manganese triazolate is pyrolyzed in highly purified N_2 , metal nitride is formed directly, rather than via a manganese metal phase. This result is strikingly different from other published studies on the pyrolysis of MOFs, where the metal ions initially form metal clusters or nanoparticles.^[2a-c,3,4] The Fourier transform of EXAFS spectra (Figure 1c) shows a decrease in the Mn–N distance during pyrolysis,^[24] which results from the transformation from manganese triazolate (Mn–N 2.16 Å) to Mn_2N_x (1.98 Å) (Scheme 1a).

When conducting in situ scanning transmission electron microscopy (STEM) imaging to observe the morphology evolution during the pyrolysis of the MOF, it was found that the pyrolysis evolved quite differently in the high-vacuum conditions of the STEM chamber (10^{-7} mbar). Both the element mapping (**Figure 2**) and elemental content analysis based on electron energy

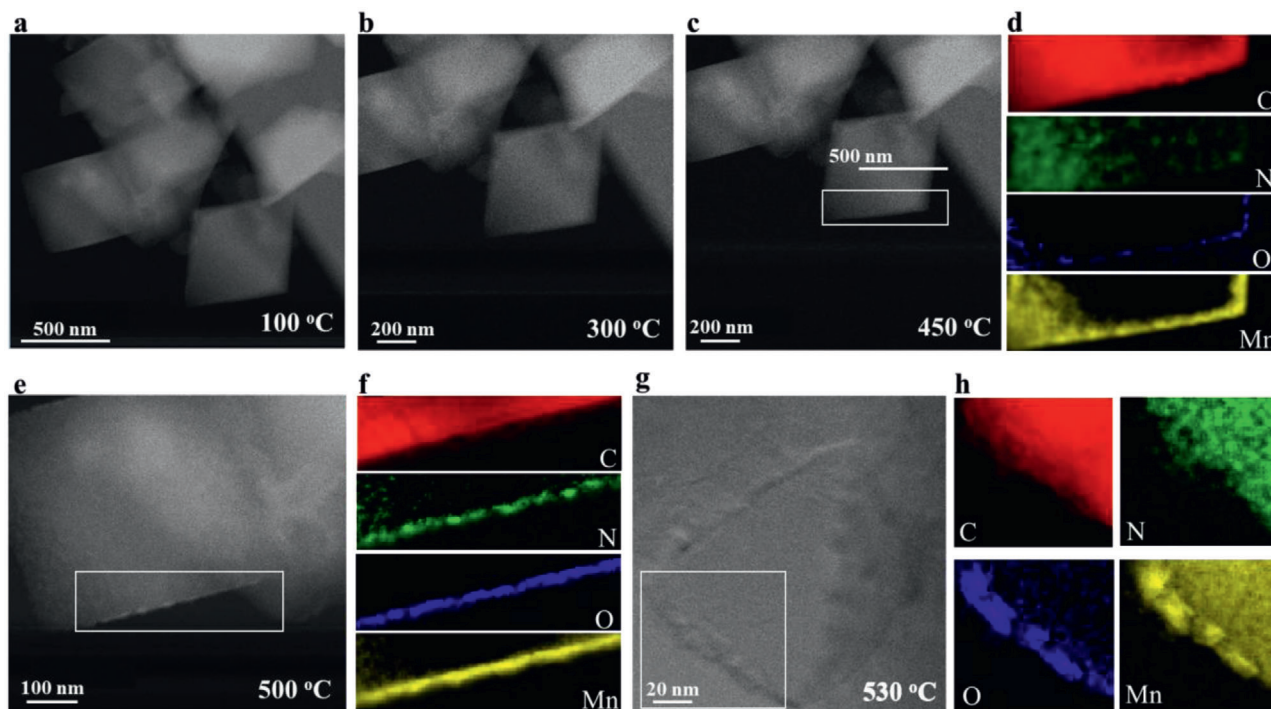


Figure 2. a–g) In situ STEM images when manganese triazolate was heated up from room temperature with a ramp rate of $5\text{ }^{\circ}\text{C min}^{-1}$: at 100, 300, 450, 500, and 530 $^{\circ}\text{C}$, respectively; d, f, h) Energy-dispersive X-ray spectroscopy element mappings of the boxed area in (c), (e), and (g), respectively.

loss spectroscopy (Figure S5, Supporting Information) show that N is gradually lost (especially at the surface) before any nitride is formed. Upon losing N, Mn^{2+} quickly scavenged the residual oxygen inside the STEM chamber,^[25] eventually forming manganese oxide nanoparticles on the surface of the original MOF. Energy-dispersive X-ray spectroscopy (EDS) element mappings indicate that manganese oxide starts to form at 500 $^{\circ}\text{C}$, as O starts to accumulate at the edge and the signals from Mn and O overlaps (Figure 2e–h). It seems likely that, under high-vacuum conditions, nitride could not be formed because nitrogen was lost as N_2 or NH_3 even before the temperature reached 400 $^{\circ}\text{C}$, while the manganese triazolate is thermally stable at this temperature under atmospheric pressure. It has previously been reported that the decomposition temperatures of certain organic molecules are lower in high-vacuum conditions.^[26] We conclude that the thermal stability of manganese triazolate is much lower in high-vacuum conditions compared with atmospheric pressure, leading to very different pyrolysis behavior.

Thermogravimetric analysis-mass spectrometry (TG-MS) was employed to further probe the pyrolysis mechanism of manganese triazolate. The same temperature ramp rate of $5\text{ }^{\circ}\text{C min}^{-1}$ and N_2 flow rate of 100 mL min^{-1} were used. A notable CH_4 peak and a very weak NH_3 peak accompanied the drop in mass at $\approx 500\text{ }^{\circ}\text{C}$, followed by an N_2 peak at $\approx 550\text{ }^{\circ}\text{C}$ (Figure 1d). Surprisingly, when conducted in air, manganese metal and triazole ($\text{C}_2\text{H}_3\text{N}_3$) were detected (Figure S6, Supporting Information). In addition, the decomposition temperature in air is lower than that in N_2 at various ramp rates (Figure 1b). This implies that the existence of oxygen or moisture might catalyze the decomposition of the MOF into metal and the linker molecules. The different results in N_2 and in air indicate that the manganese triazo-

late's pyrolysis is significantly affected by the atmosphere. Two other metal triazolates were also synthesized: the Fe- and Co-based ones (MET-3 and MET-4).^[17] However, these metal triazolates could not be converted into metal nitrides through the same heat treatment as the manganese triazolate. Instead, iron carbide (Fe_3C) and cobalt metal were formed from MET-3 and MET-4, respectively (Figure S7, Supporting Information). Thus, apart from the reaction conditions, other factors such as the metal itself also affect the pyrolysis products of MOFs; such behavior is worthy of further study.

There are two possible pathways for the manganese nitride to be formed during the pyrolysis in N_2 . First, metallic Mn could be formed before reacting with N_2 to make the manganese nitride; this would be similar to what has been reported for other MOF pyrolysis.^[2a–c] For bulk Mn metal, a temperature as high as 750 $^{\circ}\text{C}$ is necessary for N_2 to oxidize Mn to manganese nitride.^[27] Considering the nanoscale of the metal particles formed from MOFs, a lower temperature might be sufficient. However, the formation of metal is not detected by either XRD or XAFS when the manganese triazolate is pyrolyzed in highly purified N_2 . To completely eliminate the possibility of Mn metal reacting with the N_2 atmosphere to form manganese nitride, control runs of pyrolysis/annealing were done in Ar gas and the same Mn_2N_x nanocrystals were formed (Figure S8, Supporting Information). In addition, the formation of manganese nitride started at around 510 $^{\circ}\text{C}$ based on the in situ XAFS analysis, while N_2 peak was detected at $\approx 550\text{ }^{\circ}\text{C}$ by TG-MS. Thus, the possibility of Mn metal reacting with released N_2 from the MOF to form manganese nitride is rather low.

In light of the above findings on the phase transformation and identification of the products from the pyrolysis reaction, a

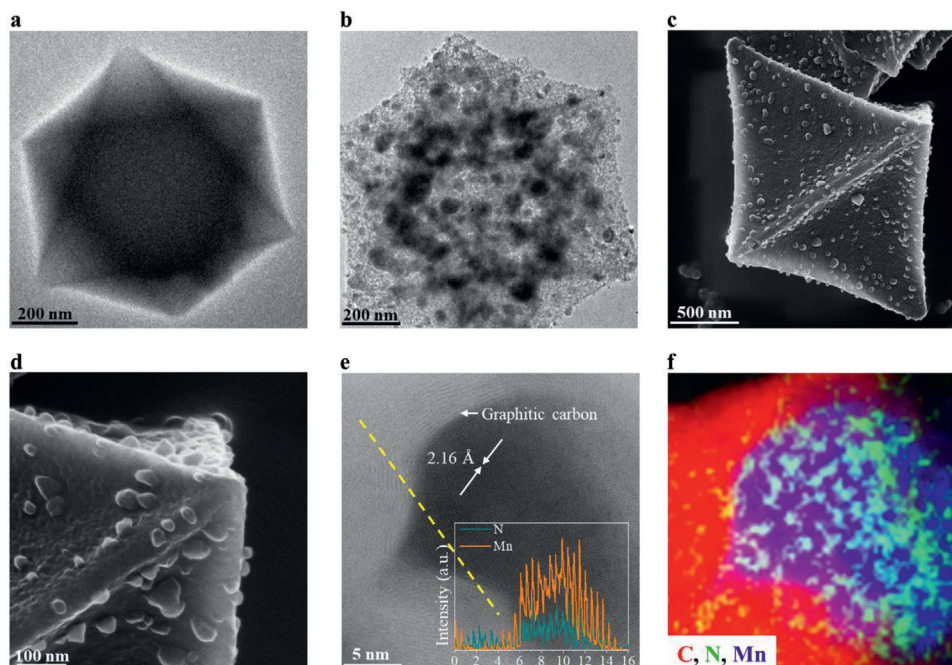


Figure 3. Morphology and chemical composition evolution from manganese triazolate to the manganese nitride/carbon hybrid. TEM images of the a) as-synthesized manganese triazolate and b) MN/NGC. c,d) Helium ion microscopy (HIM) images of MN/NGC from different directions. e) High-resolution TEM image of MN/NGC showing the lattice fringes of both Mn_2N_x and graphitic carbon layer (inset shows the Energy-dispersive X-ray spectroscopy line scan results of N and Mn along the yellow line). f) Elemental mapping of (e).

second pathway is proposed: the direct transformation from manganese triazolate into manganese nitride. More precisely, the triazole molecule linked to Mn^{2+} decomposes at around 500 °C during the pyrolysis, beginning with N–N bond cleavage that causes ring-opening of the triazolate, which is energetically feasible.^[28] Small molecules such as CH_4 are released and the N atoms form metal nitride with Mn^{2+} at the same time as the triazole bond cleavage. N_2 is released at a higher temperature when the N and C-containing fragments further decompose, giving rise to the N_2 peak at around 550 °C in Figure 1d and leaving amorphous carbon behind (see illustration in Scheme 1b). During the pyrolysis/annealing at 525 °C, N_2 is not released but N-doped carbon is obtained. As evidence in support of this proposal, the chemical analysis (using CHNS analyzer and inductively coupled plasma-optical emission spectrometer) shows a lower N at% in the products when the annealing temperature is higher than 550 °C (Table S1, Supporting Information). The simplified overall reaction is proposed in Scheme 1a, based on which the Gibbs free energy (G_d) for the decomposition was calculated (Table S2, Supporting Information). The negative G_d shows that the pyrolysis of the MOF into Mn_2N (Mn_2N_x is simplified into Mn_2N for calculation purpose), C (graphite), CH_4 , and N_2 is energetically favored.

Chemical analysis revealed the hybrid nature of the pyrolysis product MN/NGC, confirming that it contains both Mn_2N_x nanocrystallites and N-doped carbon (Table S1, Supporting Information). Around 57 at% of N from the MOF transferred into manganese nitride while the remaining exist as N atoms that are doped in the graphitic carbon layer or the amorphous carbon monolith. The global morphology does not change greatly

upon pyrolysis (Figure 3 and Figure S9, Supporting Information). The manganese triazolate crystals are octahedra, 0.5 to 2 μm in size when viewed by scanning electron microscopy (Figure S9a, Supporting Information), while the 2D imaging by transmission electron microscopy (TEM) shows a hexagonal projection (Figure 3a). After pyrolysis, the octahedral monoliths are maintained (Figure 3b), but helium ion microscopy (HIM) imaging clearly shows that nanoparticles of around 30 nm are formed on the surface of the original manganese triazolate (Figure 3c,d and Figure S10, Supporting Information). The original octahedra shrank to form octahedral carbon monoliths with sunken surfaces (Figure 3b–d). When the manganese triazolate collapses, it appears that the Mn^{2+} may diffuse to the surfaces of the octahedra and react with the N atoms, as the system is N-rich. The nanocrystallites of Mn_2N_x grow on the surface to minimize surface energy and N-doped carbon is left behind in the bulk. High-resolution TEM imaging and EDS element mapping (Figure 3e,f) show that the nanoparticles are fully covered by N-doped carbon layers and reveal lattice fringes corresponding to the (111) plan of $Mn_2N_{0.86}$ (powder diffraction file (PDF) No. 31-0824). The morphology evolution is summarized in Scheme 1b.

To assess the boundary conditions and limiting size of the manganese nitride in maintaining its stability in air, the products obtained from different pyrolysis/annealing temperatures and durations were examined. Upon increasing the annealing time from 4 to 6 h at the original temperature of 525 °C where MN/NGC was obtained, the oxygen content in the final product increased significantly (Table S1, Supporting Information). When examining its morphology using TEM (Figure S11, Supporting Information), it was found that when annealing time is

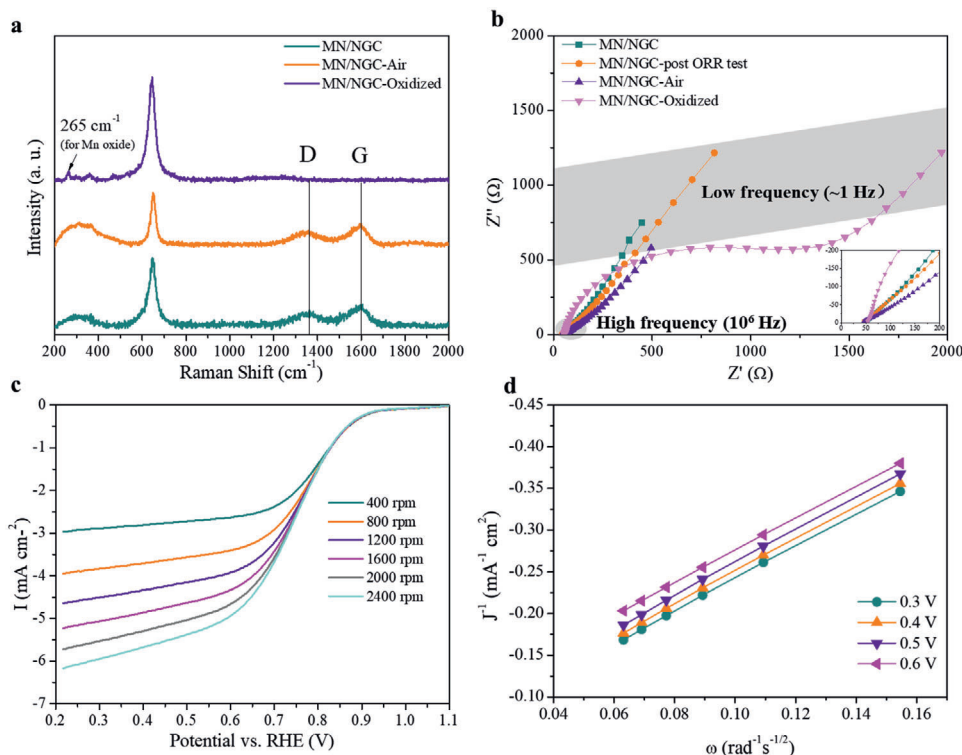


Figure 4. Characterizations of the manganese nitride/carbon hybrid and the oxidized samples. a) Raman spectrum and b) Nyquist plots for various samples; c) Polarization curves at different rotation speeds and d) Koutecky–Levich plots from 0.3 to 0.6 V (vs RHE) for MN/NGC.

extended from 4 to 6 h, the manganese nitride particles become bigger (from ≈ 30 nm to more than 50 nm) and the coverage of the graphitic carbon layer tends to be incomplete. In addition, some particles with lattice fringes corresponding to Mn_3O_4 are observed. The Mn_3O_4 is formed as a result of the oxidation of manganese nitride as soon as it comes into contact with air while being retrieved from the tube furnace. It is thus concluded that the graphitic-carbon layers could not withstand annealing for 6 h, most probably due to the crystal growth of manganese nitride nanoparticles.^[29] The MN/NGC was kept in air to examine its air-stability. After four weeks in air (MN/NGC-air), the dominant crystal structure is still $\text{Mn}_2\text{N}_{0.86}$, while three small peaks at 34.9° , 40.5° , and 58.7° 2θ appeared (Figure S12, Supporting Information), which are associated with crystalline MnO (PDF No. 07-0230). The MnO is probably formed from residual Mn^{2+} left in the bulk of the octahedron, as Mn_3O_4 is the product when Mn_2N_x is oxidized in air.

Pure manganese nitride is highly reactive toward oxygen and is readily oxidized.^[30] Indeed, when synthesizing bulk manganese nitride (Mn_3N_2) based on a reported method,^[31] it is difficult to avoid oxidation (Figure S13, Supporting Information). When higher annealing temperatures are used for the original duration of 4 h, the graphitic-carbon layer formed at around 525°C could not be retained at all and the manganese nitride nanoparticles were oxidized into mixture of Mn_3O_4 and Mn_2N_x as soon as they came in contact with air (Figures S14 and S15, Supporting Information), similar to the bulk Mn_3N_2 we synthesized. Thus, the size of the nitride particle is crucial in maintaining the integrity of the carbon layer so that oxidation can be prevented. In this case,

30 nm is the limiting size of the manganese nitride nanoparticles in maintaining the graphitic layer's integrity, therefore maintaining the stability of manganese nitride nanoparticle in air.

The $\text{Mn}_2\text{N}_{0.86}$ (111) thin film is a ferromagnetic material^[32] and the electronic structure of crystalline $\text{Mn}_2\text{N}_{0.86}$ confirms its metallic nature.^[33] Thus, bulk $\text{Mn}_2\text{N}_{0.86}$ has an electrical conductivity that is much higher than that of most metal oxides. The layered structure of the carbon in Figure 3e, with its uniform interlayer distance, suggests that it is graphitic in nature. This is confirmed by the Raman spectrum of the MN/NGC, which shows the higher intensity of the G band compared with the D band (Figure 4a),^[34] while containing defects due to the N-doping^[35] and curvature. The carbon monolith left after collapse of the MOF acts as a scaffold to hold the manganese nitride nanoparticles, maximizing their surface area. As a result, these manganese nitride nanoparticles, which are enclosed in graphitic-carbon layers and supported by the carbon monolith, have potential interest for applications that require both catalytic activity of a transition-metal nitride and high electrical conductivity. To explore this possibility, the ORR electrocatalytic activity of MN/NGC was tested and compared with samples that are oxidized to various extents.

For a better comparison between the manganese nitride and oxide in terms of electrical conductivity, a sample of MN/NGC was treated in an oven at 300°C under air flowing for controlled oxidation (MN/NGC-oxidized). The octahedral carbon monolith was retained, even though the nitride was fully oxidized to Mn_3O_4 (Figure S16, Supporting Information) and the overall carbon content is not largely affected (Table S1, Supporting Information). The Nyquist plots obtained from electrical impedance

spectroscopy show that, due to complete oxidation through heat treatment in air, the electron transfer resistance of MN/NGC-oxidized becomes much larger (Figure 4b). However, by being exposed to air for over four weeks or going through the ORR test, the electrical conductivity of the MN/NGC is hardly affected. The high electrical conductivity of the manganese nitride nanoparticles and the fact that they are uniformly distributed on the surface of the carbon monolith contributed to the diffusion-dominant impedance profile. The ORR activities in an O₂-saturated alkaline aqueous solution were examined by linear sweep polarization and the onset potential at 1600 rpm was used to represent the ORR catalytic activity. The onset potential of MN/NGC is significantly higher than the oxidized control sample and comparable or higher than the reported values for manganese oxide-based catalysts (Figure S18, Supporting Information).^[36] At 1600 rpm, the onset potential of Mn/NGC is 928 mV, comparable with the one for Pt/C (10 wt%) tested at same condition (932 mV, Figure S19a, Supporting Information). The limiting current increases linearly when the rotation speed is increased from 400 to 2400 rpm (Figure 4c). The perfectly linear Koutecky–Levich plots (Figure 4d) from 0.3 to 0.6 V (vs RHE) and the parallel fitted lines suggest first-order reaction kinetics toward the concentration of dissolved oxygen.^[37] The electron transfer number calculated using slopes of the Koutecky–Levich plots is ≈ 4 , meaning the nearly complete reduction of O₂. These parameters demonstrate the high catalytic efficiency of the manganese nitride nanoparticles obtained. The fact that the nanoparticles are supported on the relative large carbon monolith resulted in a less direct contact between the nanoparticles and the rotating-disk electrode.^[38] Therefore, the half-wave potential of MN/NGC is lower than the one for Pt/C (Figure S19, Supporting Information). The graphitic carbon with a thickness of several layers does not affect the accessibility of electrolyte accessibility. In fact, an appropriate carbon coating has been a very effective way to improve the electrical conductivity, and maintain the core's chemical stability of the core phase in energy storage and catalysis applications.^[39]

The pyrolysis of MOFs has become an important strategy for developing functional nanomaterials. In the present work, we have conducted a thorough mechanistic study on the pyrolysis of manganese triazolite, Mn(C₂N₃H₂)₂. New insights of the pyrolysis of MOF were gained, in terms of phase transformation, reaction pathways, and morphology evolution under different reaction conditions, which opens up new possibilities for MOF-derived functional nanomaterials. Interestingly, the pyrolysis carried out in an oxygen-free environment with precise process control leads to the formation of a nanoscale and air-stable manganese nitride (Mn₂N_x), of which the synthesis has always been a challenge. The resulting Mn₂N_x nanoparticles of around 30 nm in diameter were closely embedded in nitrogen-doped graphitic carbon layers and uniformly distributed on a carbon monolith. The existence of the graphitic carbon layers and the size match between the two species is key to prevent manganese nitride from being oxidized. In addition, the manganese nitride nanocrystallites are good electrical conductors. Thus, they show promising performance when tested for ORR electrocatalysis.

The reaction pathway of pyrolysis depends not only on the reaction conditions (e.g., whether in pure N₂, air, or high-vacuum environment) but also on the metal species of MOF. While the manganese triazolite gives rise to direct nitride formation, pyro-

lysis of the Fe and Co analogues results in the formation of Fe₃C and cobalt metal, respectively. Such phenomenon is worthy of further study.

Experimental Section

Chemicals used, experimental details, in situ studies, and all characterization methods can be found in the Supporting Information.

Supporting Information

Supporting Information is available from the Wiley Online Library or from the author.

Acknowledgements

The authors acknowledge the support by Singapore Ministry of Education, Tier 1 grant (R284-000-193-114) and the Green Energy Programme (R284-000-185-731) supported by the National University of Singapore.

Conflict of Interest

The authors declare no conflict of interest.

Keywords

air-stable nanoparticles, electrocatalysis, metal–organic frameworks, pyrolysis, transition-metal nitrides

Received: August 21, 2020

Revised: September 30, 2020

Published online: January 4, 2021

- [1] a) Z. Liang, C. Qu, W. Guo, R. Zou, Q. Xu, *Adv. Mater.* **2018**, *30*, 1870276; b) H. F. Wang, L. Chen, H. Pang, S. Kaskel, Q. Xu, *Chem. Soc. Rev.* **2020**; c) Q. Wang, D. Astruc, *Chem. Rev.* **2020**, *120*, 1438; d) H. Zhang, X. Liu, Y. Wu, C. Guan, A. K. Cheetham, J. Wang, *Chem. Commun.* **2018**, *54*, 5268.
- [2] a) C. Guan, A. Sumboja, H. Wu, W. Ren, X. Liu, H. Zhang, Z. Liu, C. Cheng, S. J. Pennycook, J. Wang, *Adv. Mater.* **2017**, *29*, 1704117; b) Y. Li, R. Wang, T. Wang, X.-F. Cheng, X. Zhou, F. Fei, X.-S. Wang, *Angew. Chem., Int. Ed.* **2017**, *129*, 15638; c) K. Nakatsuka, T. Yoshii, Y. Kuwahara, K. Mori, H. Yamashita, *Chem. Eur.* **2018**, *24*, 898; d) M. Zhang, Q. Dai, H. Zheng, M. Chen, L. Dai, *Adv. Mater.* **2018**, *30*, 1705431.
- [3] R. Das, P. Pachfule, R. Banerjee, P. Poddar, *Nanoscale* **2012**, *4*, 591.
- [4] a) B. Chen, G. Ma, Y. Zhu, Y. Xia, *Sci. Rep.* **2017**, *7*, 5266; b) V. P. Santos, T. A. Wezendonk, J. J. D. Jaén, A. I. Dugulan, M. A. Nasalevich, H.-U. Islam, A. Chojecki, S. Sartipi, X. Sun, A. A. Hakeem, A. C. J. Koeken, M. Ruitenbeek, T. Davidian, G. R. Meima, G. Sankar, F. Kapteijn, M. Makkee, J. Gascon, *Nat. Commun.* **2015**, *6*, 6451.
- [5] a) K. Xi, S. Cao, X. Peng, C. Ducati, R. V. Kumar, A. K. Cheetham, *Chem. Commun.* **2013**, *49*, 2192; b) C. Wang, J. Kim, J. Tang, J. Na, Y.-M. Kang, M. Kim, H. Lim, Y. Bando, J. Li, Y. Yamauchi, *Angew. Chem., Int. Ed.* **2020**, *59*, 2066.
- [6] M. D. Meganathan, S. Mao, T. Huang, G. Sun, *J. Mater. Chem. A* **2017**, *5*, 2972.
- [7] a) M. Hu, S. Zhao, S. Liu, C. Chen, W. Chen, W. Zhu, C. Liang, W.-C. Cheong, Y. Wang, Y. Yu, Q. Peng, K. Zhou, J. Li, Y. Li, *Adv. Mater.* **2018**, *30*, 1801878; b) H. He, Y. Cui, B. Li, B. Wang, C. Jin, J. Yu, L. Yao, Y. Yang, B. Chen, G. Qian, *Adv. Mater.* **2019**, *31*, 1806897.

- [8] a) A. Li, Y. Tong, H. Song, X. Chen, *J. Phys. Chem. C* **2018**, *122*, 17278; b) P. Pachfule, D. Shinde, M. Majumder, Q. Xu, *Nat. Chem.* **2016**, *8*, 718; c) L. Oar-Arteta, T. Wezendonk, X. Sun, F. Kapteijn, J. Gascon, *Mater. Chem. Front.* **2017**, *1*, 1709; d) W. Chen, J. Pei, C. T. He, J. Wan, H. Ren, Y. Wang, J. Dong, K. Wu, W. C. Cheong, J. Mao, X. Zheng, W. Yan, Z. Zhuang, C. Chen, Q. Peng, D. Wang, Y. Li, *Adv. Mater.* **2018**, *30*, 1800396; e) F. Liu, S. Liu, J. Meng, F. Xia, Z. Xiao, Z. Liu, Q. Li, J. Wu, L. Mai, *Nano Energy* **2020**, *73*, 104758.
- [9] W. Xia, A. Mahmood, Z. Liang, R. Zou, S. Guo, *Angew. Chem., Int. Ed.* **2016**, *55*, 2650.
- [10] J. S. Lee, D. J. Ham, in *Encyclopedia of Catalysis* (Ed: I. Horvath), Wiley, Ann Arbor, MI **2010**.
- [11] M.-S. Balogun, Y. Huang, W. Qiu, H. Yang, H. Ji, Y. Tong, *Mater. Today* **2017**, *20*, 425.
- [12] a) D. R. Deng, F. Xue, Y. J. Jia, J. C. Ye, C. D. Bai, M. S. Zheng, Q. F. Dong, *ACS Nano* **2017**, *11*, 6031; b) K. R. Yoon, K. Shin, J. Park, S.-H. Cho, C. Kim, J.-W. Jung, J. Y. Cheong, H. R. Byon, H. M. Lee, I.-D. Kim, *ACS Nano* **2018**, *12*, 128; c) T. Varga, G. Ballai, L. Vászrhelyi, H. Haspel, Á. Kukovecz, Z. Kónya, *Appl. Catal., B* **2018**, *237*, 826; d) H. Zhang, D. Tian, Z. Zhao, X. Liu, Y. Hou, Y. Tang, J. Liang, Z. Zhang, X. Wang, J. Qiu, *Energy Storage Mater.* **2019**, *21*, 210.
- [13] N. Zhang, Y. Zou, L. Tao, W. Chen, L. Zhou, Z. Liu, B. Zhou, G. Huang, H. Lin, S. Wang, *Angew. Chem., Int. Ed.* **2019**, *58*, 15895.
- [14] T. Zhou, W. Lv, J. Li, G. Zhou, Y. Zhao, S. Fan, B. Liu, B. Li, F. Kang, Q.-H. Yang, *Energy Environ. Sci.* **2017**, *10*, 1694.
- [15] Z. Sun, J. Zhang, L. Yin, G. Hu, R. Fang, H.-M. Cheng, F. Li, *Nat. Commun.* **2017**, *8*, 14627.
- [16] W. Sun, C. J. Bartel, E. Arca, S. R. Bauers, B. Matthews, B. Orvañanos, B.-R. Chen, M. F. Toney, L. T. Schelhas, W. Tumas, J. Tate, A. Zakutayev, S. Lany, A. M. Holder, G. Ceder, *Nat. Mater.* **2019**, *18*, 732.
- [17] F. Gándara, F. J. Uribe-Romo, D. K. Britt, H. Furukawa, L. Lei, R. Cheng, X. Duan, M. O'Keeffe, O. M. Yaghi, *Chem. Eur.* **2012**, *18*, 10595.
- [18] G. Zapf, K. Dalal, *Mod. Dev. Powder Metall.* **1977**, *10*, 129.
- [19] R. Niewa, Z. Hu, R. Kniep, *Eur. J. Inorg. Chem.* **2003**, *2003*, 1632.
- [20] J. S. Vrettos, G. W. Brudvig, in *Comprehensive Coordination Chemistry II* (Eds: J. A. McCleverty, T. J. Meyer), Pergamon, Oxford **2003**, Ch. 8.
- [21] J. McBreen, *Handbook of Solid State Batteries and Capacitors*, World Scientific, Singapore **1995**.
- [22] E. Céspedes, Y. Huttel, L. Martínez, A. de Andrés, J. Chaboy, M. Vila, N. D. Telling, G. van der Laan, C. Prieto, *Appl. Phys. Lett.* **2008**, *93*, 252506.
- [23] Y. Gorlin, B. Lassalle-Kaiser, J. D. Benck, S. Gul, S. M. Webb, V. K. Yachandra, J. Yano, T. F. Jaramillo, *J. Am. Chem. Soc.* **2013**, *135*, 8525.
- [24] J. Li, M. Chen, D. A. Cullen, S. Hwang, M. Wang, B. Li, K. Liu, S. Karakalos, M. Lucero, H. Zhang, C. Lei, H. Xu, G. E. Sterbinsky, Z. Feng, D. Su, K. L. More, G. Wang, Z. Wang, G. Wu, *Nat. Catal.* **2018**, *1*, 935.
- [25] T. Arockiadoss, *US WO/2012/143763*, **2012**.
- [26] A. A. Koptelov, S. V. Karyazov, *Dokl. Phys. Chem.* **2003**, *389*, 101.
- [27] R. D. W. Kemmitt, in *The Chemistry of Manganese, Technetium and Rhenium* (Eds: R. D. W. Kemmitt, R. D. Peacock), Pergamon, Oxford **1973**, Ch. 37.
- [28] J. Ghosh, A. Bhattacharya, *Chem. Phys.* **2016**, *464*, 26.
- [29] H. S. Chin, L. S. Chao, *J. Nanomater.* **2013**, *2013*, 424953.
- [30] C. Walter, P. W. Menezes, S. Orthmann, J. Schuch, P. Connor, B. Kaiser, M. Lerch, M. Driess, *Angew. Chem., Int. Ed.* **2018**, *57*, 698.
- [31] A. Leineweber, R. Niewa, H. Jacobs, W. Kockelmann, *J. Mater. Chem.* **2000**, *10*, 2827.
- [32] G. L. Wang, M. Meng, W. Q. Zhou, Y. J. Wang, S. X. Wu, S. W. Li, *Mater. Lett.* **2016**, *184*, 291.
- [33] a) H. J. Goldschmidt, *Interstitial Alloys*, Butterworth-Heinemann, Oxford **1967**; b) R. Yu, X. Chong, Y. Jiang, R. Zhou, W. Yuan, J. Feng, *RSC Adv.* **2015**, *5*, 1620.
- [34] Y. Su, S. Li, D. Wu, F. Zhang, H. Liang, P. Gao, C. Cheng, X. Feng, *ACS Nano* **2012**, *6*, 8349.
- [35] Y. Mao, H. Duan, B. Xu, L. Zhang, Y. Hu, C. Zhao, Z. Wang, L. Chen, Y. Yang, *Energy Environ. Sci.* **2012**, *5*, 7950.
- [36] a) T. Zhang, S. Zhang, S. Cao, Q. Yao, J. Y. Lee, *Chem. Mater.* **2018**, *30*, 8270; b) W. Xiang, Y. Zhao, Z. Jiang, X. Li, H. Zhang, Y. Sun, Z. Ning, F. Du, P. Gao, J. Qian, K. Kato, M. Yamauchi, Y. Sun, *J. Mater. Chem. A* **2018**, *6*, 23366; c) T. Zhang, Z. Li, P. Sun, L. Wang, X. Niu, S. Wang, *Catal. Today* **2019**. d) Y. Gu, G. Yan, Y. Lian, P. Qi, Q. Mu, C. Zhang, Z. Deng, Y. Peng, *Energy Storage Mater.* **2019**, *23*, 252.
- [37] Y. Lu, Y. Jiang, X. Gao, X. Wang, W. Chen, *J. Am. Chem. Soc.* **2014**, *136*, 11687.
- [38] C. Wang, L. Ma, L. Liao, S. Bai, R. Long, M. Zuo, Y. Xiong, *Sci. Rep.* **2013**, *3*, 2580.
- [39] a) L. Sun, R. Li, W. Zhan, Y. Yuan, X. Wang, X. Han, Y. Zhao, *Nat. Commun.* **2019**, *10*, 2270; b) W. An, B. Gao, S. Mei, B. Xiang, J. Fu, L. Wang, Q. Zhang, P. K. Chu, K. Huo, *Nat. Commun.* **2019**, *10*, 1447.